Supplementary Materials for

Nanoparticle-Directed Bimodal Crystallization of the Quasi-1D van der Waals Phase, Bi$_4$I$_4$

S. J. Allison[1], D. L. M. Cordova[1], M. Hasib[1], T. Aoki[2], M. Q. Arguilla[1]*

Affiliations:

[1]Department of Chemistry, University of California Irvine; Irvine, California 92697, USA

[2]Irvine Materials Research Institute, University of California Irvine; Irvine, California 92697, USA

*Corresponding author. Email: marguill@uci.edu

This PDF file includes:

Materials and Methods

Supplementary Discussion

Supplementary Results

Figures S1 to S17

Tables S1 to S13

Supplementary References

Materials and Methods

Materials preparation and handling

All commercially available materials were used as received unless otherwise noted. All air- and water-sensitive reagents and samples were stored inside an Ar-filled glove box when not in use.

Chemical vapor deposition synthesis of Bi_4I_4 nanostructures

Bi_4I_4 was grown through a chemical vapor deposition (CVD) technique. In the syntheses of Bi_4I_4 nanostructures, a home-made CVD system based on an ambient-pressure OTF-1200x horizontal two-zone furnace (MTI Corp.) equipped with a 24"-long quartz reaction tube was used. Powders of Bi (STREM Chemicals, 99.9%) and HgI_2 (STREM Chemicals, 99+%) were mixed and placed in a 100 mm x 17 mm x 10 mm quartz boat (MTI Corp.). The stoichiometric loading ratios between the two precursors were varied throughout the study and denoted as "Bi:I". The boat containing the precursors was placed just outside of zone T_1 while a 6 cm x 1.5 cm SiO_2/Si substrate (300 nm thermal oxide; prime grade; University Wafer, Inc.) was placed in the center of zone T_2 (Fig. S1). The entire reaction vessel was evacuated to 50 mTorr and flushed with an Ar (95.0%) / H_2 (5.0%) gas mixture (Praxair) twice. [1] Under a constant Ar/H_2 gas flow rate of 78 s.c.c.m., the furnace zones were heated to pre-set temperatures (referred to as T_1 and T_2 in the manuscript) at a 10 °C per minute ramp-up rate. A constant 50 °C temperature difference was programmed between zones T_1 and T_2. Upon reaching the pre-set synthesis temperature and after a 10-minute equilibration time, the boat with the Bi and HgI_2 precursors was shuttled into zone T_1. Typical reaction times for the syntheses presented in this study are 5 minutes at the pre-set zone temperature, followed by a rapid quench to room temperature by opening the reaction furnace and elevating the reaction tube in air under an Ar/H_2 gas flow rate of 78 s.c.c.m..

Gold nanoparticle deposition on SiO_2/Si substrates

Gold nanoparticles (BBI Solutions, gold colloids) were deposited on the growth substrates using established literature procedures. [2] In a typical substrate preparation procedure, 6 cm x 1.5 cm SiO_2/Si substrates (300 nm thermal oxide; prime grade; University Wafer, Inc.) were sonicated in Millipore water, acetone, and isopropanol at 5 minutes in each solution followed by blow-drying under N_2 gas. The as-cleaned substrates were then pre-wetted with a poly-L-lysine solution (Sigma-Aldrich, 0.1% w/v in H_2O) and rinsed with Millipore H_2O. Colloidal suspensions of gold nanoparticles (Au NPs; diameter = 100 nm, 50 nm, 20 nm, or 5 nm; BBI Solutions) were then uniformly drop-cast on the pre-treated substrates. The resulting poly-L-lysine-Au NP-treated substrates were subsequently rinsed with Millipore H_2O and blow-dried under N_2 gas.

Chemical vapor transport synthesis of bulk Bi_4I_4 crystals

Bulk crystals of Bi_4I_4 used as reference in this study were synthesized following a modified methodology previously reported in literature. [3] In brief, powders of Bi (STREM Chemicals, 99.9%) and HgI_2 (STREM Chemicals, 99+%) were mixed and sealed in a Pyrex borosilicate ampoule under a < 50 mTorr base pressure. The ampoule is then placed in an OTF-1200x horizontal two-zone furnace (MTI Corp.) wherein both temperature zones were first heated to 240 °C at a 10°C/min ramp-up rate. Upon reaching 240°C, hot zone temperature is then raised to 300 °C over the course of 5 hours while keeping the cold zone at 240°C. Typical reactions were run at these temperatures (300°C/240°C) for 14 days followed by slow cooling to room temperature over the course of 24 hours. This growth method results in fibrous and needle-like single crystals of Bi_4I_4 as confirmed by Raman spectroscopy and electron backscatter diffraction.

Optical microscopy and Substrate Mapping

High magnification (up to 100x) optical images of as grown and micromechanically exfoliated crystals were collected on an Olympus BX43F microscope with BF and DF capabilities. Low-magnification images (up to 5x) of single crystals were collected on a Zeiss B2000C stereo microscope equipped with both top and bottom illumination sources.

As shown in Figure 2d and S14, the resulting nanocrystals from CVD growth substrates were mapped in 1 mm^2 spatial increments by using a 50x objective to record the boundaries of the different regions in the substrate which resulted in different Bi_xI_x crystalline morphologies and identities. Our procedure for mapping the growth substrates is as follows: First, the (x,y) coordinates of the growth substrate corners were recorded to provide boundaries for the substrate map. The substrate was then scanned in 1 mm^2 increments starting at one of the substrate corners. Our optical microscope is equipped with a joystick with micromechanical control and a digital readout, which provided the ability to precisely scan in x and y directions down to the nearest 0.01 μm. Within each 1 mm^2 region, the morphology and density of the nanostructures were recorded. The maps were color coded as follows: light brown for Bi_4I_4 1D nanowires, dark brown for Bi_4I_4 2D nanosheets, and black for BiI_3 crystals. The growth of the 1D nanowires was extremely dense across most of the growth substrate, therefore, any region marked in light brown contains many hundreds of nanowires. Regions with > 25 nanosheets were marked in dark brown. For the undiluted 20 nm Au NP growths, > 50 nanosheets were observed in many of the dark brown regions. 1 mm^2 regions with > 0 BiI_3 nanocrystals observed were marked in black.

Scanning Transmission Electron Microscopy and selected-area electron diffraction

High-Angle Annular Dark-Field Scanning Transmission Electron Microscopy (HAADF-STEM) images and selected-area electron diffractograms (SAED) were acquired using a JEOL Grand ARM 300CF equipped with double Cs-correctors, a cold field-emission source, and Gatan GIF Quantum/K2 operated at an accelerating voltage of 300 kV. EDS elemental maps were acquired through JEOL's Dual 100 mm^2 SDDs and were processed using the Gatan DigitalMicrograph® software. Samples were prepared by smearing lacey carbon TEM grids on the resulting growth substrates. Analysis of raw HAADF-STEM data (.dm4) was done using Gatan DigitalMicrograph® software. FFT processing of the micrographs were done using the ImageJ software. Indexing of SAED and FFT data were performed using the SingleCrystal software (CrystalMaker®).

Scanning Electron Microscopy and Energy-Dispersive X-Ray Spectroscopy

Scanning electron microscopy (SEM) imaging and Energy-dispersive X-Ray Spectroscopy (EDS) analyses were performed using a FEI Magellan 400 XHR SEM, equipped with an ETD detector and an 80 mm^2 Oxford silicon drift EDS detector. Imaging and EDS analysis were done at an operating voltage of 10-20 kV and current of at least 0.2 nA. EDS spectra reported for Au NPs throughout the manuscript were taken on the growth substrate surface post-reaction. Au NPs (N ≥ 10) of similar shapes and sizes were selected from representative areas of the growth substrate for the representative conditions presented in the study. The resulting EDS spectra were analyzed using the AZtec software. Standard deviation was calculated to determine percent error in EDS measurements. [4] Due to the resolution of EDS measurements and its dependence on the sample type and morphology, the reported EDS % composition values were mainly used for qualitative and comparative purposes to establish trends observed in the syntheses.

Electron Backscatter Diffraction

Electron backscatter diffraction (EBSD) images and Kikuchi patterns were taken using a FEI Quanta 3D FEG dual beam equipped with a phosphorous screen detector. All measurements were performed on Bi_4I_4 nanocrystals transferred from the growth substrate using a polydimethylsiloxane (PDMS; SYLGARD™ 184, Dow Corning) stamp. The diffractograms of the nanostructures under study were taken at an operating voltage of 20 kV and current of at least 1 nA. Kikuchi patterns were indexed using HKL Fast Acquisition software using a model Bi_4I_4 structure file.

Grazing Incidence X-ray Diffraction

The grazing incidence X-ray diffraction (GI-XRD) pattern of the as-grown Bi_4I_4 nanostructures on an SiO_2/Si substrate was collected using a Rigaku SmartLab X-ray diffractometer equipped with a Cu Kα source and a 1D D/tex Si strip detector in a grazing incidence angle thin film configuration. The incoming X-ray photons were incident on the sample at a 0.2° angle. The Bi_4I_4 nanostructures used for this experiment was synthesized using the following reaction conditions: 20 nm Au NPs; $T_1 = 320$ °C / $T_2 = 270$ °C temperature setting; 4:3 Bi:I precursor ratio; 78 s.c.c.m. Ar/H_2 (5%) gas flow rate; and 5 minutes reaction time. The simulated powder XRD patterns of Bi_4I_4 needle/plate morphologies with (010)/(001) preferred orientation were used as a reference pattern for indexing.

Atomic Force Microscopy

Atomic force microscopy (AFM) images were collected on an Anton Paar Tosca 400 AFM using non-contact mode Arrow™ Silicon SPM Sensor tips with a nominal tip size of 10 nm, resonance frequency of 285 kHz, and force constant of 42 N/m (NanoWorld). For AFM measurements, Bi_4I_4 nanocrystals were mechanically transferred using PDMS from the growth substrate to 300 nm SiO_2/Si substrates with fiduciary markings. The resulting micrographs were processed and analyzed using the Gwyddion® software.

Micro-Raman Spectroscopy

Raman spectra were collected using a Renishaw InVia Raman microscope system equipped with a CCD detector, 532 nm laser, and a 1200 mm^{-1} grating. Raman spectroscopy measurements were performed with a nominal laser power of 0.103 mW, 10 s exposure time, and 1-5 accumulations.

Temperature Calibration of Growth Substrates

The temperature of the growth substrate was calibrated using an external temperature probe. The probe was inserted into a clean quartz tube used previously in a Bi_4I_4 CVD reaction. One side of the quartz tube was attached to the Ar/H_2 gas inlet valve. The other end of the quartz tube was attached to a T-valve that allowed for the outflow of Ar/H_2 gas as well as the insertion of the temperature probe. Ar/H_2 gas was flowed into the quartz tube at the same flow rate as used in all Bi_4I_4 experiments, 78 s.c.c.m. Both furnace zones were heated to the target temperature at 5 °C/min and then the temperature was allowed to stabilize for 30 min once the maximum temperature was reached. The temperature was then taken at 0.5 cm increments, starting at the furnace center. The temperature was stabilized for 10 minutes at each position before the temperature was recorded.

Due to the temperature differences observed between the furnace thermocouple and the temperature probe, an additional temperature calibration was performed. No quartz tube was

placed in the furnace, instead, insulating blocks were placed at the furnace edges. A flexible temperature probe was then threaded through the blocks and placed in close contact to the furnace thermocouple in the growth zone. At a furnace setting of 320 / 270 °C, the temperature of the probe was 264.1 °C. This is in clear contrast to the previous temperature calibration performed (Fig. S2) and highlights the combined effects of the quartz tube, Ar/H_2 gas flow, and open tube ends on the temperature of the growth substrate. Because the Bi_4I_4 CVD reactions were run with these conditions, the temperature calibration data provided in Fig. S2 more accurately reflects the actual temperatures of the different regions of the growth substrate than does the temperature of the furnace thermocouple.

Supplementary Discussion

Resulting Bi_4I_4 nanostructures under non-optimal conditions

Looking at the temperature-dependence of the resulting nanostructures (Fig. 2a, second from left column), at a 4:3 Bi-to-I ratio, increasing the programmed furnace temperature to $T_1 = 340^oC$ / $T_2 = 290^oC$ produced clusters of 10-20 μm long Bi_4I_4 nanowires and nanoribbons with varying cross-sectional areas and BiI_3 nucleation cores. On the other hand, still at a 4:3 Bi-to-I ratio, lower furnace temperatures programmed at $T_1 = 300^oC$ / $T_2 = 250^oC$ resulted in the formation of BiI_3, "Bi_3I", and Bi_4I_4 nanocrystals. Further decreasing these set temperatures to $T_1 = 250^oC$ / $T_2 = 200^oC$ yielded recrystallized HgI_2 precursors on the substrate surface. Complementarily looking into the dependence of the resulting nanostructures on the precursor Bi-to-I ratios, at $T_1 = 320^oC$ / $T_2 = 270^oC$ (Fig. 2a, second from the top row), decreasing the Bi:I ratio from 4:4 to 4:1 by stoichiometric amounts of iodine produced BiI_3, pure phase Bi_4I_4, BiI_3 and Bi_4I_4, and amorphous Bi_xI_y (x≠y), respectively.

Influence of Bi lone pair in the growth along [100]-direction

From a crystallographic standpoint, the probable influence of the *6s* Bi lone pairs can be inferred from the anisotropic inter-chain Bi—I distances wherein the shortest distance (corresponding to stronger interactions) falls on the [100]-direction (Fig. S16). This bonding motif is reminiscent of the interaction of stereochemically active *5s* lone pairs of Sb in Sb-based q-1D vdW crystals with adjacent electronegative atoms. [5, 6] These interactions have been shown to direct the preferred crystallization of nanostructures and thin films along crystallographic directions parallel to the direction of the lone pair-lone pair interactions. [7, 8] In contrast to the Bi—I interactions along the [100]-direction, lateral Bi atoms oriented along the perpendicular [001]-direction (*c*-axis) are characterized by a 5-coordinate geometry and are not likely to interact with the adjacent-chain I atoms. These results suggest that significantly stronger inter-chain interactions along the [100]-direction (*a*-axis) between the stereochemically active lone pair of Bi and the more electronegative I atom could influence the preferred crystallization of the nanosheets along this crystallographic direction.

Formation of elongated Bi_4I_4 quasi-2D nanosheets

We show that control over the morphologies of the resulting quasi-2D nanosheets can be achieved by slight variations in the precursor Bi-to-I ratios. Analysis of the surface atoms for the different crystalline faces of β-Bi_4I_4, shows that there are an equal number of bismuth and iodine atoms along the [100]-direction, while there are two iodine atoms for every one bismuth atom on the [001]-direction. As the "equistoichiometric" Au NPs are observed to dissolve equal amounts of bismuth and iodine, the direction of growth is most favorable for the 1:1 Bi:I [100]-direction rather than the 1:2 Bi:I [001]-direction. To support this, we show that when the precursor ratio Bi:I is decreased from 4:3 to 4:2, nanosheets with a significantly higher aspect ratio of 10(3) (4:2 Bi-to-I) were observed to form (Fig. 2a; Table S13). This is in stark contrast to nanosheets with an aspect ratio of 2.3(4) formed when the Bi-to-I precursor ratio is 4:3. Here, aspect ratio is defined as sheet base to tip divided by the widest point on the crystal. With more bismuth than iodine atoms available for the 4:2 Bi-to-I reaction conditions, the growth rate along the 1:1 Bi:I [100]-direction is faster than the 2:1 Bi:I [001]-direction resulting in significantly narrower nanosheets.
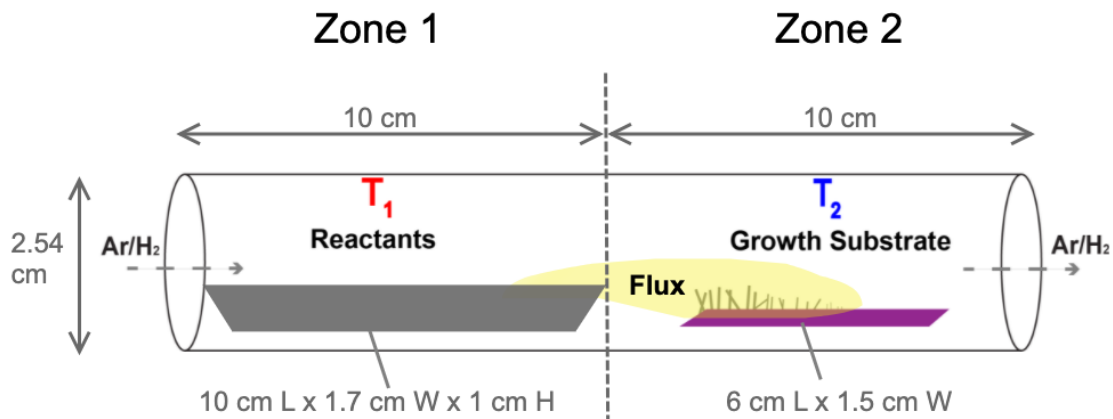
Supplementary Results

Figure S1. Schematic of the home-built CVD system used for the synthesis of Bi_4I_4 nanostructures. The schematic which includes the configuration, dimensions, distances, and positions of the reactant boat (in gray) and growth substrate (in purple) with respect to the CVD tube and temperature zones (T_1 and T_2).

Table S1. Position-dependent calibration of the growth zone temperature. Thermocouple readings taken at 0.5 cm increments from substrate edge closest to precursor (hot/left edge of the substrate in Zone T_2) at various T_1/T_2 temperature program settings used in the study.

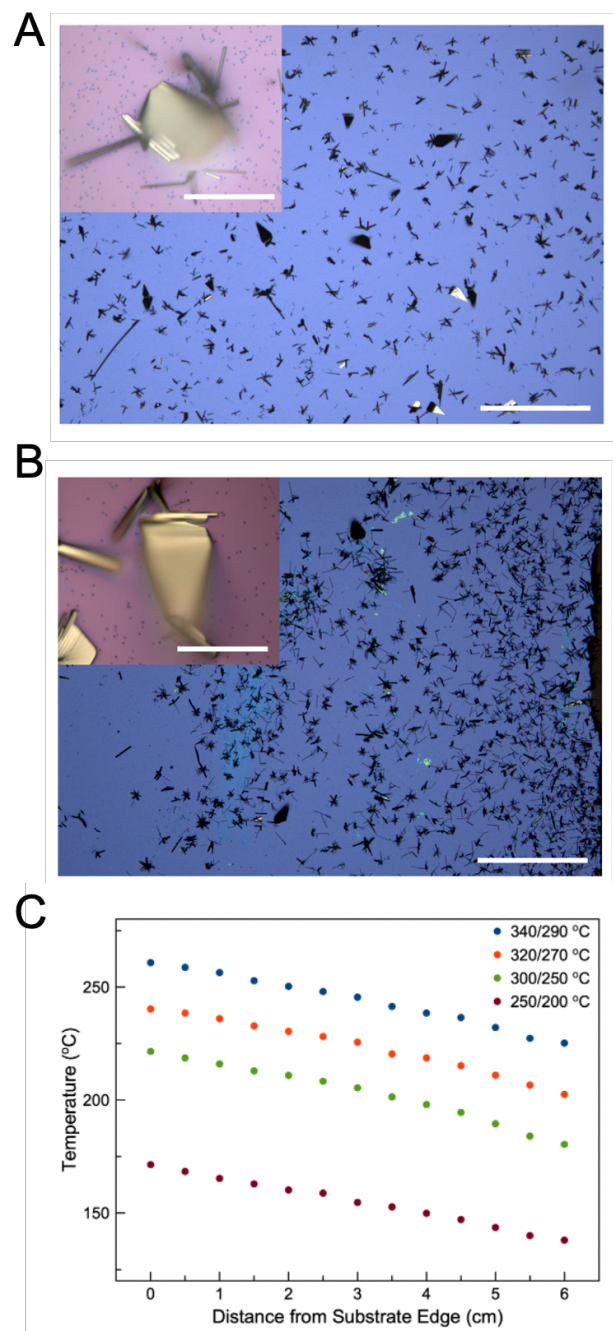| Distance From Edge (cm)	$T_1/T_2 = 340/290$°C Temperature (°C)	$T_1/T_2 = 320/270$ °C Temperature (°C)	$T_1/T_2 = 300/250$°C Temperature (°C)	$T_1/T_2 = 250/200$°C Temperature (°C)
0.0	260.8	240.3	221.5	171.4
0.5	258.7	238.5	218.6	168.4
1.0	256.4	236.0	216.0	165.3
1.5	252.8	232.8	212.9	162.9
2.0	250.3	230.4	210.9	160.2
2.5	248.0	228.1	208.3	158.8
3.0	245.5	225.6	205.4	154.7
3.5	241.4	220.4	201.4	152.7
4.0	238.5	218.6	198.0	149.9
4.5	236.5	215.2	194.5	147.1
5.0	232.1	211.0	189.5	143.6
5.5	227.3	206.6	184.0	140.0
6.0	225.2	202.5	180.4	138.0

Figure S2. Specific synthetic conditions for CVD-grown Bi_4I_4 nanocrystals. (A) Optical images of Bi_4I_4 nanostructures grown from CVD reaction with 78 s.c.c.m. Ar / H_2 (5%) gas flow rate. (B) Optical images of Bi_4I_4 nanostructures grown from CVD reaction with 78 s.c.c.m. Ar gas flow rate. The following conditions were used in both reactions: 100 nm Au NPs; $T_1 = 320$ °C / $T_2 = 270$ °C temperature setting; 4:3 Bi:I precursor ratio; 5 minute reaction time. Scale bars 245 μm (large image), 25 μm (inset). (B) Temperature versus distance plot of the calibrated growth zone (T_2) furnace temperatures across the region where the SiO_2/Si growth substrates were positioned shown as a graphical representation of the calibration data shown in in Table S1. The graph shows temperature readings at various distances from the hot (left side) edge of the substrate from the various T_1/T_2 program settings used in the growth reactions presented in this study.

Table S2. Gaussian peak fitting results of the Raman spectral peaks (position and FWHM) observed in the spectra shown in Fig. 1d. The Raman shifts fitted from these peaks correspond to the B_g (100.0 cm^{-1}) and A_g (115.6 cm^{-1}) phonon modes of Bi_4I_4 and the A_g (113.9 cm^{-1}) phonon mode of BiI_3 reported in literature. [9, 10]

Crystal	Peak 1		Peak 2	
	Position (cm^{-1})	FWHM	Position (cm^{-1})	FWHM
Bulk Bi_4I_4	100.0	11.25	115.6	6.72
Bulk BiI_3	113.9	10.09	-	-

Table S3. Elemental composition of the resulting on-substrate 100 nm Au NPs taken post-reaction. The atomic percentages of Bi, I, and Au from EDS measurements are presented. **Reaction conditions resulting in the Au NPs analyzed:** 100 nm Au NPs; T_1 = 300ºC / T_2 = 250ºC temperature setting; 4:4 Bi:I precursor ratio; 78 s.c.c.m. Ar/H_2 (5%) gas flow rate; and 5 minutes reaction time.

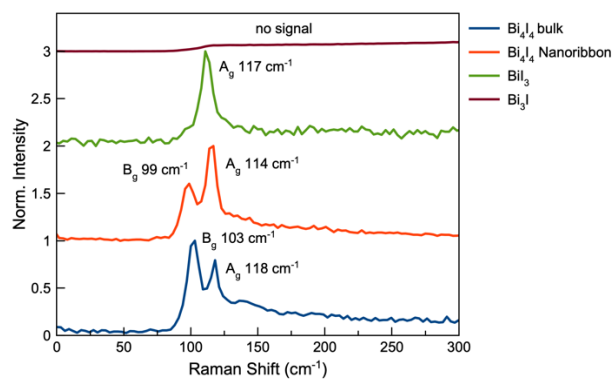| Nanoparticle	% Bismuth	% Iodine	% Gold
1	10	7	83
2	11	9	80
3	7	5	88
4	15	6	79
5	8	7	85
6	9	7	84
7	9	5	86
8	12	6	82
9	6	2.6	91
10	19	18	63
Average ± Std. Dev.	11 ± 4	7 ± 4	82 ± 8
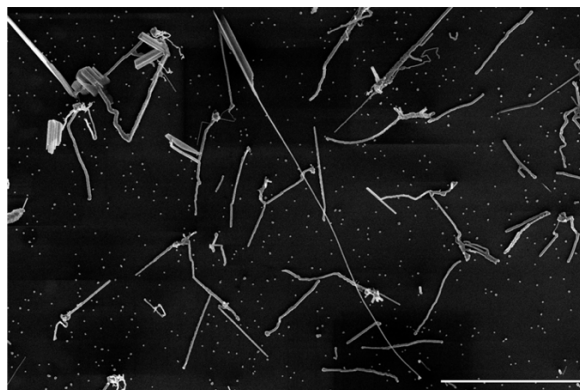
Figure S3. (left) Raman spectra of various as-grown Bi_xI_y nanostructures. The graph shows bulk Bi_4I_4 crystals, Bi_4I_4 nanoribbon grown from CVD, BiI_3 nanosheet grown from CVD, and "Bi_3I" nanowire grown from CVD. Peak assignments were based on reported literature values. [9, 10] (right) SEM image of "Bi_3I" nanowires grown from CVD. The micrograph depicts the kinked and non-uniform morphology of the nanowires. A long and uniform Bi_4I_4 nanowire could also be seen running along the middle portion of the micrograph. Scale bar, 20 μm. **Reaction conditions resulting in the nanostructures:** 100 nm Au NPs; $T_1 = 320$ °C / $T_2 = 270$ °C temperature setting; 4:4 Bi:I precursor ratio; 78 s.c.c.m. Ar/H$_2$ (5%) gas flow rate; and 5 minutes reaction time.

Table S4. Elemental composition of representative Bi_xI_y nanostructures found on the growth substrate post-synthesis. The atomic percentages of Bi and I from EDS measurements are presented. These results show growth of Bi_4I_4, BiI_3, and "Bi_3I" (Bi_xI_y where $x > y$) nanostructures under these specific reaction conditions. **Reaction conditions resulting in the Bi_xI_y nanostructures analyzed:** 100 nm Au NPs; $T_1 = 300$ °C / $T_2 = 250$ °C temperature setting; 4:4 Bi:I precursor ratio; 78 s.c.c.m. Ar/H_2 (5%) gas flow rate; and 5 minutes reaction time.

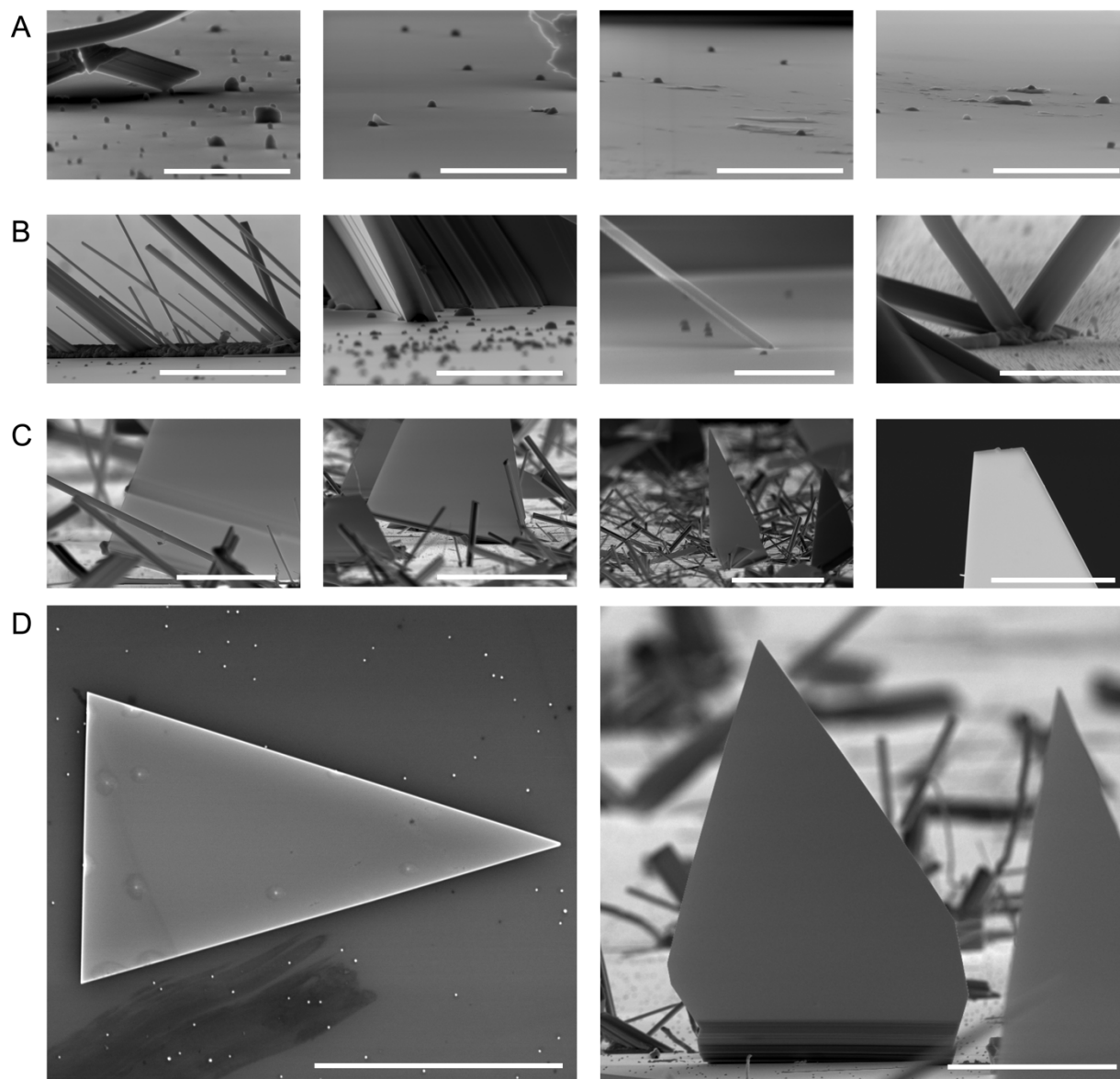| Phase (Morphology)	Bi %	I %
Bi_4I_4 (Wire) 1	50.1	49.9
Bi_4I_4 (Wire) 2	51.2	48.8
Bi_4I_4 (Nanosheet) 1	49.6	50.4
Bi_4I_4 (Nanosheet) 2	49.1	50.9
Bi_4I_4 (Nanosheet) 3	50.4	49.5
"Bi_3I" (Wire) 1	75.5	24.5
"Bi_3I" (Wire) 2	75.3	24.7
BiI_3 (Nanosheet)	27.6	72.4

Figure S4. Representative SEM images of various nanostructures resulting from the growth of Bi$_4$I$_4$ at various reaction conditions. The micrographs were taken at an 88° angle from substrate surface. (A) Micrographs depicting nanoparticles with amorphous growth and deposition on substrate surface. Scale bars (left to right), 1 μm, 2 μm, 2 μm, and 2 μm. (B) Micrographs illustrating Bi$_4$I$_4$ nanowires that either grow radially from a single nucleation point or protruding at an angle from the substrate. Scale bars (left to right), 4 μm, 2 μm, 1 μm, and 1 μm. (C) Micrographs that show how Bi$_4$I$_4$ nanosheets grow laterally from the facet of nanowires that protrude at an angle from the substrate. Au NPs could be found at the tip of these flag-like triangular nanosheets of Bi$_4$I$_4$. Scale bars (left to right), 10 μm, 30 μm, 50 μm, and 4 μm. (D) SEM image of a flattened Bi$_4$I$_4$ nanosheet with Au NP protrusions on the (001) surface (left) and a Bi$_4$I$_4$ nanosheet grown vertically on the growth substrate with no gold nanoparticles observed on the (001) surface (right). Scale bars 20 μm.
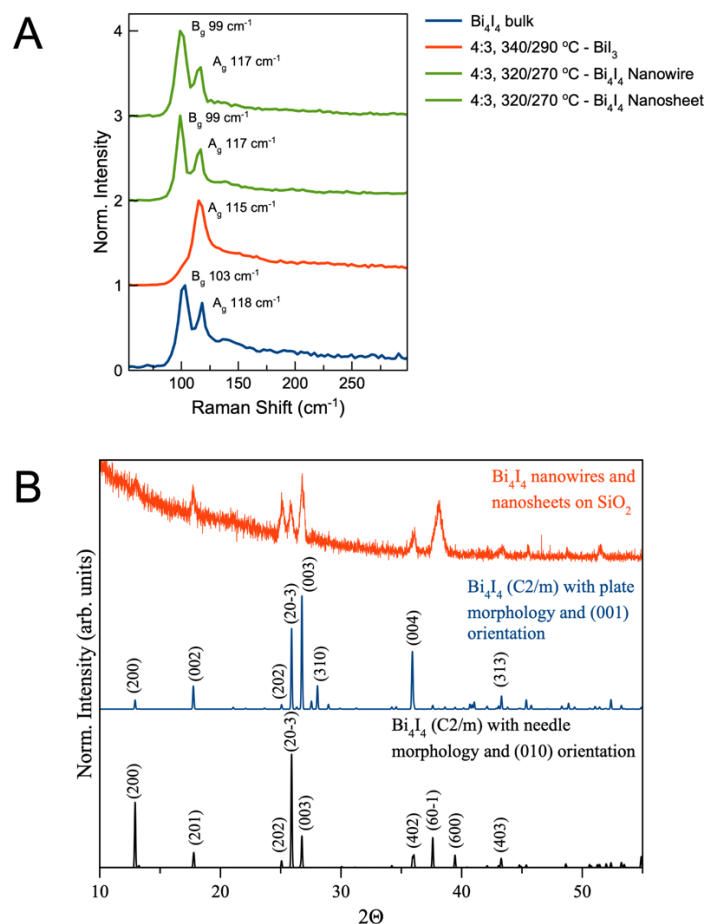
Figure S5. (A) Raman spectra of representative nanostructures obtained from various CVD growth conditions used in this study. Peak assignments were based on reported literature values. [9, 10] The legend indicates the Bi:I precursor ratios, T_1 and T_2 temperatures in the T_1/T_2 format, and the morphology of the crystals. (B) GI-XRD pattern collected with a grazing incidence angle configuration on as-grown Bi_4I_4 nanostructures on SiO_2 (top). Simulation of the powder XRD pattern of β-Bi_4I_4 with needle morphology and (010) orientation (bottom) and plate morphology and (001) orientation (middle). **Reaction conditions for GI-XRD data**: 20 nm Au NPs; $T_1 = 320$ ºC / $T_2 = 270$ ºC temperature setting; 4:3 Bi:I precursor ratio; 78 s.c.c.m. Ar/H_2 (5%) gas flow rate; and 5 minutes reaction time.

Table S5. Elemental composition of representative nanostructures and crystals obtained from the various CVD reaction conditions used in the study. The atomic percentages of Bi, I, and Hg from EDS measurements are presented.

| Reaction Conditions (Precursor Bi:I; T_1/T_2)	Phase	Bi %	I %	Hg %
4:3; 340/290 ºC	BiI_3 1	27.9	72.1	--
	BiI_3 2	28.6	71.4	--
	BiI_3 3	27.8	72.2	--
4:4; 320/270 ºC	BiI_3 1	27.7	72.3	--
	BiI_3 2	25.3	74.7	--
	BiI_3 3	26.7	73.3	--
4:3; 320/270 ºC	Bi_4I_4 1	48	52	--
	Bi_4I_4 2	51	49	--
%Bi (Ave. ± Std. Dev.) = 49 ± 1	Bi_4I_4 3	50	50	--
%I (Ave. ± Std. Dev.) = 51 ± 1	Bi_4I_4 4	48	52	--
	Bi_4I_4 5	49	51	--
	Bi_4I_4 6	48	52	--
4:2; 320/270 ºC	Bi_4I_4 1	51	49	--
	Bi_4I_4 2	52	48	--
	BiI_3 1	24.8	75.2	--
4:1; 320/270 ºC	Bi_xI_y 1	32	68	--
	Bi_xI_y 2	40	60	--
	Bi_xI_y 3	37	63	--
4:4; 300/250 ºC	Bi_4I_4 1	54	46	--
	Bi_4I_4 2	49	51	--
	Bi_xI_y	61	39	--
	BiI_3 1	74.3	25.7	--
4:3; 300/250 ºC	Bi_4I_4 1	46	54	--
	Bi_4I_4 2	49	51	--
	Bi_xI_y 1	65	35	--
	BiI_3 1	23.7	76.3	--
4:2; 300/250 ºC	Bi_xI_y 1	38	62	--
	Bi_xI_y 2	72.1	27.9	--
	*Bi_4I_4 3	44	56	--
4:3; 250/200 ºC	HgI_2 1	--	65.4	34.6
	HgI_2 2	--	64.9	35.1
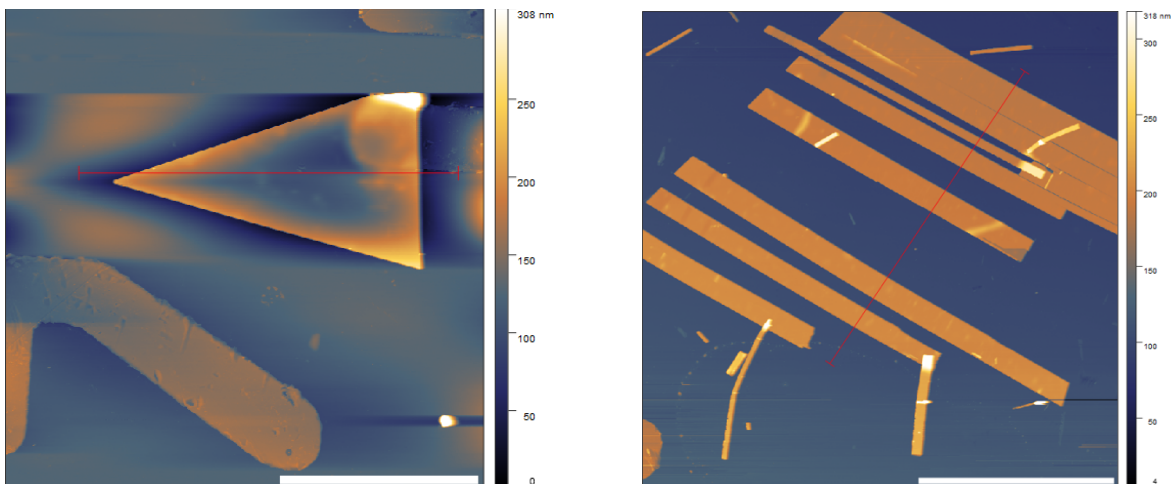
Figure S6. AFM images of representative Bi_4I_4 nanosheets that were mechanically transferred using PDMS from the growth substrate to SiO_2/Si substrates with fiduciary markings. The thicknesses of the nanosheets in the left and the right micrographs are 125 nm and 99 nm, respectively. Due to the vertical orientation of the nanosheets with respect to the plane of the substrate and the PDMS, some nanosheets cleave along the long axis of the chains (parallel to the base of the triangular nanosheet) during the transfer process as is shown in the right micrograph. Scale bars, 20 μm. The red bars indicate the region from which the height was extracted. **Reaction conditions resulting in the nanosheets:** 100 nm Au NPs (left), 50 nm Au NPs (right); $T_1 = 320$ °C / $T_2 = 270$ °C temperature setting; 4:3 Bi:I precursor ratio; 78 s.c.c.m. Ar/H_2 (5%) gas flow rate; and 5 minutes reaction time.
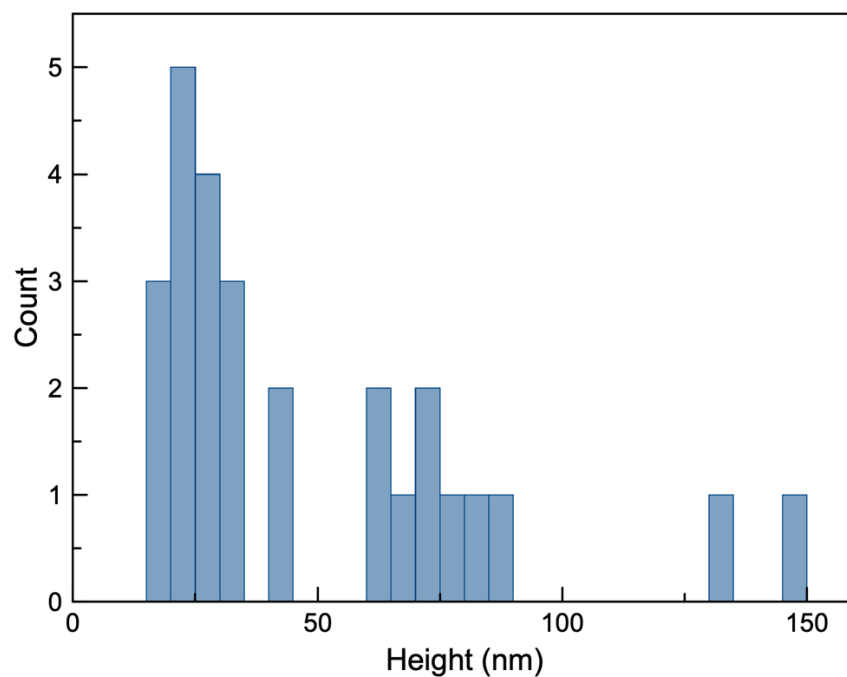
Figure S7. Thickness histogram of 27 representative Bi_4I_4 nanowires grown *via* CVD. The thicknesses were derived from AFM height measurements of individual nanowires. For these measurements, the nanowires were mechanically transferred using PDMS from the growth substrate to SiO_2/Si substrates with fiduciary markings prior to performing AFM scans. **Reaction conditions resulting in the nanowires analyzed:** 50 nm Au NPs; T_1 = 320 °C / T_2 = 270 °C temperature setting; 4:3 Bi:I precursor ratio; 78 s.c.c.m. Ar/H_2 (5%) gas flow rate; and 5 minutes reaction time.

Table S6. Thicknesses of representative Bi$_4$I$_4$ nanowires grown *via* CVD. The thicknesses were derived from AFM height measurements of individual nanowires. For these measurements, the nanowires were mechanically transferred using PDMS from the growth substrate to SiO$_2$/Si substrates with fiduciary markings prior to performing AFM scans. **Reaction conditions resulting in the nanowires analyzed:** 100 nm Au NPs and 5 nm Au NPs; T$_1$ = 320 °C / T$_2$ = 270 °C temperature setting; 4:3 Bi:I precursor ratio; 78 s.c.c.m. Ar/H$_2$ (5%) gas flow rate; and 5 minutes reaction time.

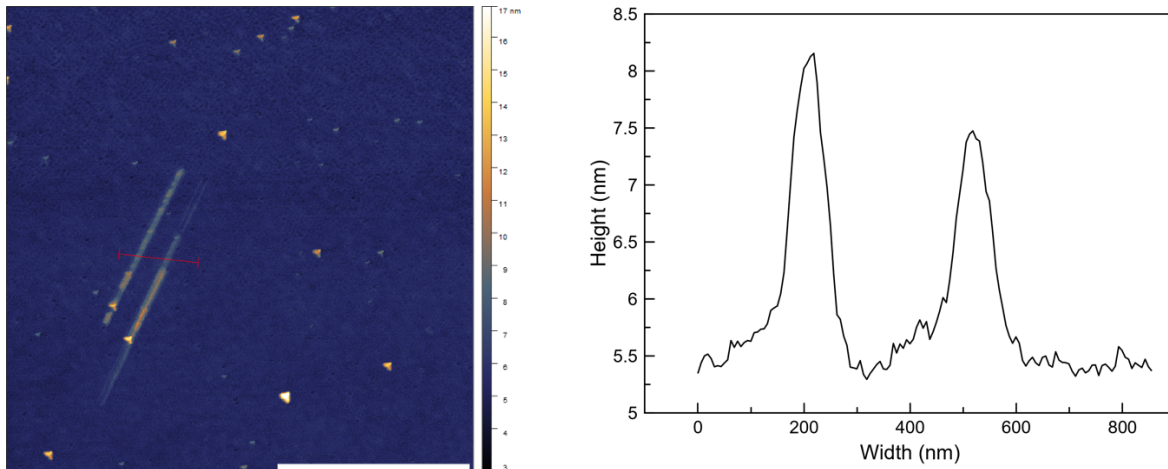| Nanowire # (5 nm Au NPs)	Height (nm)	Nanowire (100 nm Au NPs)	Height (nm)
Wire 1	1.8	Wire 1	15.2
Wire 2	2.3	Wire 2	15.7
Wire 3	8.4	Wire 3	17.8
Wire 4	8.6	Wire 4	24.1
Wire 5	9.8	Wire 5	24.7
Wire 6	19.2	Wire 6	57.8
Wire 7	23.6	Wire 7	140
Wire 8	25.6	Wire 8	360
Wire 9	25.9		
Wire 10	29.8		
Wire 11	30.2		
Wire 12	41.1		
Wire 13	57.6		
Wire 14	64.9		
Wire 15	67.3		
Wire 16	105		
Wire 17	203		

Figure S8. AFM image (left) and corresponding height profile (right) of ~2 nm-thick Bi_4I_4 nanowires mechanically transferred using PDMS from the growth substrate to a SiO_2/Si substrate with fiduciary markings prior to AFM scan. Scale bar, 2 μm. The red bar indicates the region from which the height profile was extracted. There is a possibility that these nanowires were micromechanically exfoliated from a larger parent nanowire from the growth substrate. The micrograph is shown to demonstrate that very thin nanowires could be accessed, either directly or indirectly, from the growth substrates. **Reaction conditions resulting in nanowires analyzed:** 100 nm Au NPs, 5 nm Au NPs; T_1 = 320 °C / T_2 = 270 °C temperature setting; 4:3 Bi:I precursor ratio; 78 s.c.c.m. Ar/H_2 (5%) gas flow rate; and 5 minutes reaction time.

Table S7. Gaussian peak fitting results of the Raman spectral peaks (position and FWHM) observed in the spectra shown in Fig. 3d. The Raman shifts fitted from these peaks correspond to the signature Raman-active phonon modes of Bi_4I_4 in various morphologies (bulk crystal, nanoribbon, and nanosheet) with slight shifts which we attribute to Raman confinement effects. [9]

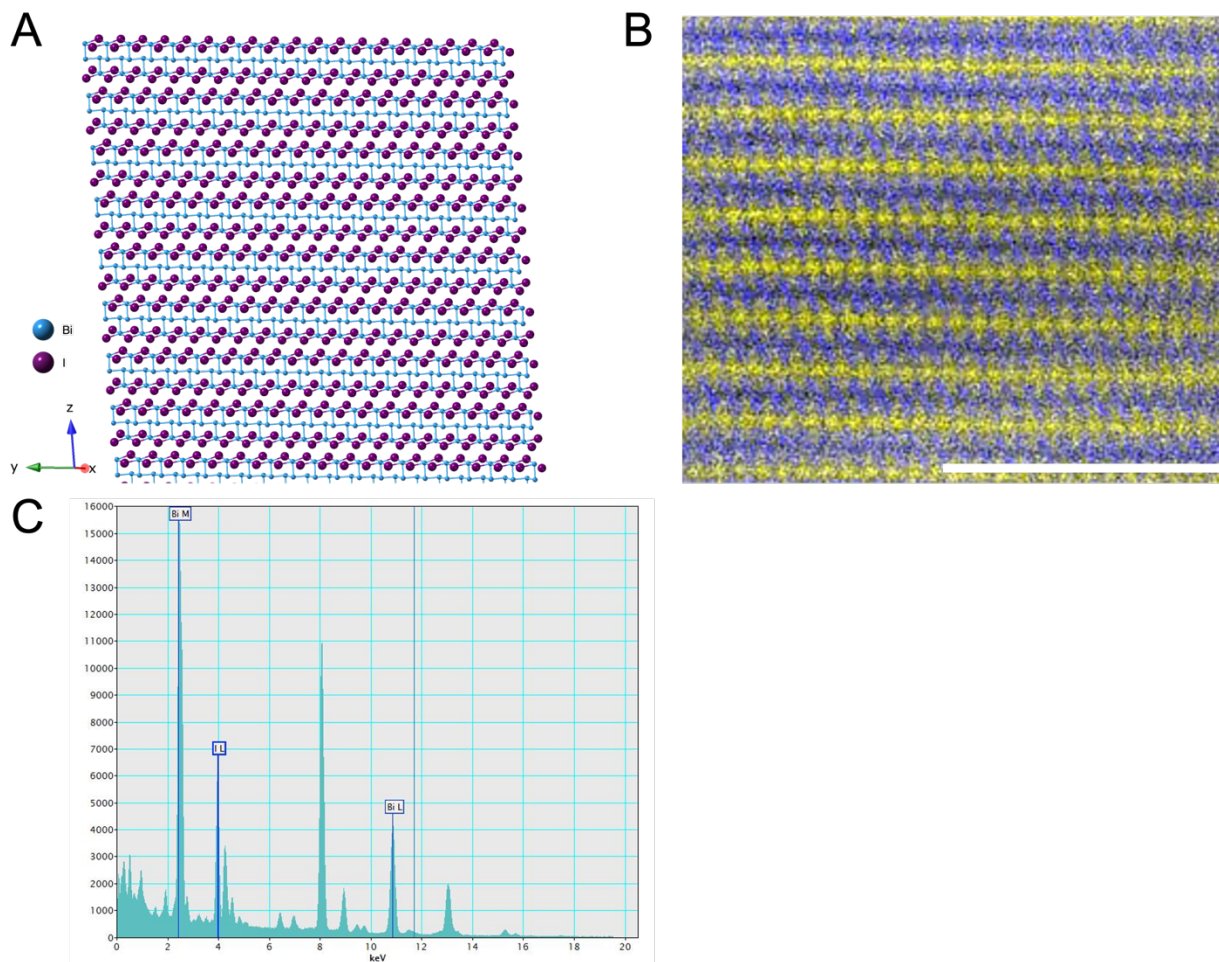| Crystal	Peak 1		Peak 2	
	Position (cm^{-1})	FWHM	Position (cm^{-1})	FWHM
Bulk Bi_4I_4	100.0	11.25	115.6	6.72
Bi_4I_4 Nanoribbon	100.0	11.18	115.6	6.76
Bi_4I_4 Nanosheet	99.7	10.78	115.4	8.04

Figure S9. (A) Crystal structure of Bi_4I_4 oriented along the [110] zone axis. Blue atoms and purple atoms correspond to bismuth and iodine, respectively. (B) High-resolution STEM-EDS elemental map of a Bi_4I_4 nanowire, scale bar 5 nm. The yellow circles/regions correspond to the $M\alpha$ line of Bi atoms while the blue circles/regions correspond to the $L\alpha$ line of the I atoms. The orientation of the crystal in this map is the same as in (A) and that of the micrograph in Fig. 3j. (C) The corresponding STEM-EDS spectrum of the nanowire shown in (b).
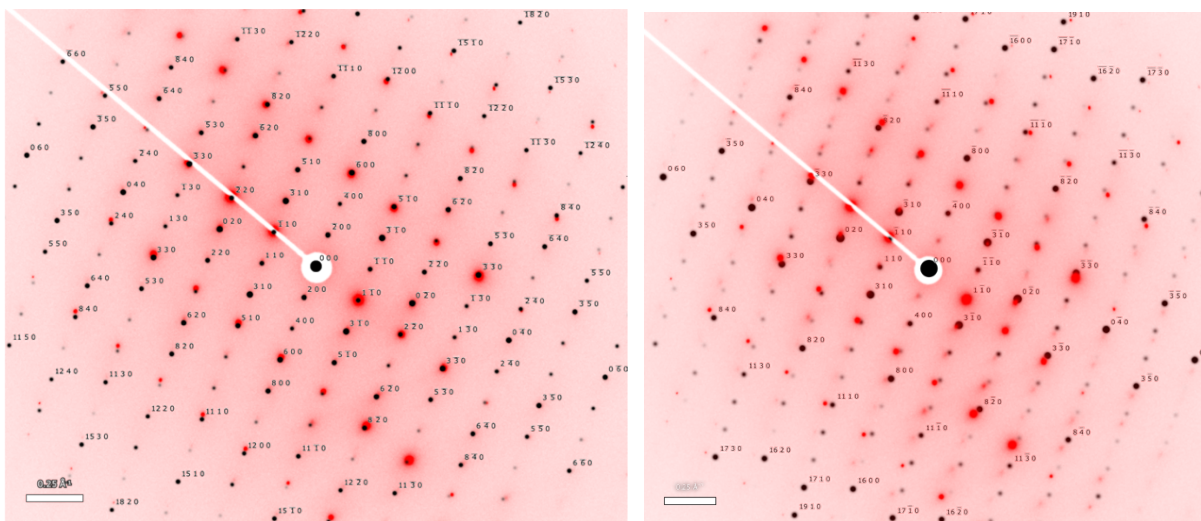
Figure S10. SAED of a Bi$_4$I$_4$ nanosheet with the electron beam normal to the wide sheet facet. The brightness and contrast of the diffractograms were adjusted for clarity. Depicted on the left is the diffractogram overlaid with the simulated diffraction pattern of β-Bi$_4$I$_4$ along the [001] zone axis which clearly shows the close agreement of the SAED pattern with the simulation. Depicted on the right is the diffractogram overlaid with the simulated diffraction pattern of α-Bi$_4$I$_4$ along the [001] zone axis which shows a noticeable pattern mismatch with the simulated diffraction pattern.
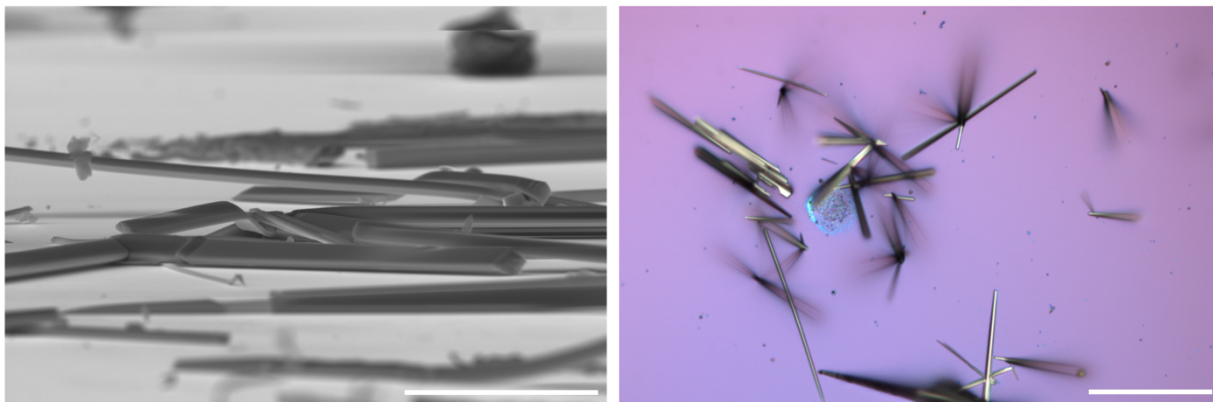
Figure S11. SEM image (left; 90º tilted; Scale bar, 10 μm) and optical micrograph (right; Scale bar, 25 μm) of the resulting growth substrate from a Bi_4I_4 CVD synthesis reaction using the optimized growth parameters but without Au NPs on substrate surface. Unlike when Au NPs are present on the substrate surface during the CVD reaction, the resulting Bi_4I_4 nanostructures mostly grow horizontally on the substrate surface. **Reaction conditions resulting in nanowires:** No Au NPs on the 300 nm SiO_2/Si substrate; T_1 = 320 ºC / T_2 = 270 ºC temperature setting; 4:3 Bi:I precursor ratio; 78 s.c.c.m. Ar/H_2 (5%) gas flow rate; and 5 minutes reaction time.
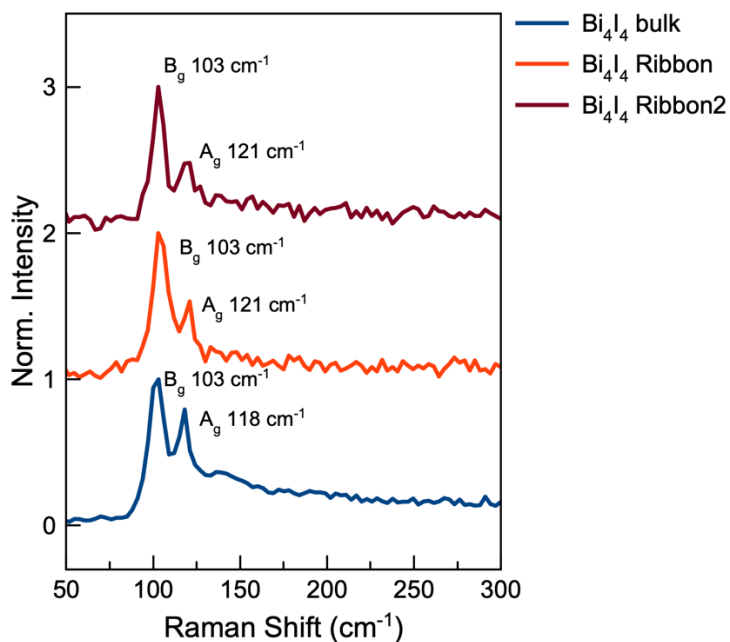
Figure S12. Raman spectra of representative Bi₄I₄ nanostructures obtained from CVD growth in the absence of Au NPs on the substrate surface. Peak assignments were based on reported literature values. [9] **Reaction conditions resulting in nanostructures analyzed:** No Au NPs on the 300 nm SiO$_2$/Si substrate; $T_1 = 320\ ^\circ$C / $T_2 = 270\ ^\circ$C temperature setting; 4:3 Bi:I precursor ratio; 78 s.c.c.m. Ar/H$_2$ (5%) gas flow rate; and 5 minutes reaction time.

Table S8. Elemental composition of the resulting on-substrate 100 nm Au NPs taken post-reaction. The atomic percentages of Bi, I, and Au from EDS measurements are shown in the table. **Reaction conditions resulting in Au NPs analyzed:** 100 nm Au NPs; $T_1 = 320$ °C / $T_2 = 270$ °C temperature setting; 4:3 Bi:I precursor ratio; 78 s.c.c.m. Ar/H_2 (5%) gas flow rate; and 5 minutes reaction time.

	Bi %	**I %**	**Au %**
Particle 1	39.1	18.9	42.0
Particle 2	37.9	1.8	60.3
Particle 3	45.0	14.0	41.0
Particle 4	39.8	10.6	49.6
Particle 5	29.8	15.9	54.3
Particle 6	62.5	12.4	25.1
Particle 7	41.3	14.9	43.8
Particle 8	38.4	11.6	49.9
Particle 9	70.6	15.7	13.7
Particle 10	43.9	23.3	32.8
Average ± Std. Dev.	45 ± 12	14 ± 6	41 ± 14

Table S9. Elemental composition of the resulting on-substrate 50 nm Au NPs taken post-reaction. The atomic percentages of Bi, I, and Au from EDS measurements are shown in the table. **Reaction conditions resulting in Au NPs analyzed:** 50 nm Au NPs; $T_1 = 320$ °C / $T_2 = 270$ °C temperature setting; 4:3 Bi:I precursor ratio; 78 s.c.c.m. Ar/H_2 (5%) gas flow rate; and 5 minutes reaction time.

	Bi %	**I %**	**Au %**
Particle 1	23.7	13.4	62.9
Particle 2	18.3	14.0	67.8
Particle 3	18.2	14.6	67.2
Particle 4	15.2	11.9	72.9
Particle 5	14.8	26.2	58.0
Particle 6	11.5	0.7	87.8
Particle 7	15.7	8.7	75.6
Particle 8	16.6	26.6	56.8
Particle 9	34.8	5.4	59.8
Particle 10	15.02	14.48	70.5
Average ± Std. Dev.	18 ± 7	14 ± 8	68 ± 9

Table S10. Elemental composition of the resulting on-substrate 20 nm Au NPs taken post-reaction. The atomic percentages of Bi, I, and Au from EDS measurements are shown in the table. **Reaction conditions resulting in Au NPs analyzed:** 20 nm Au NPs; $T_1 = 320$ °C / $T_2 = 270$ °C temperature setting; 4:3 Bi:I precursor ratio; 78 s.c.c.m. Ar/H_2 (5%) gas flow rate; and 5 minutes reaction time.

	Bi %	**I %**	**Au %**
Particle 1	13.2	11.6	75.3
Particle 2	12.7	14.8	72.3
Particle 3	8.3	13.3	78.4
Particle 4	19.1	16.5	64.5
Particle 5	9.2	15.3	75.6
Particle 6	13.3	24.0	62.7
Particle 7	17.2	13.6	69.1
Particle 8	22.6	13.0	64.4
Particle 9	19.6	18.5	61.9
Particle 10	14.7	9.4	75.9
Average ± Std. Dev.	15 ± 4	15 ± 4	70 ± 6

Table S11. Elemental composition of the resulting on-substrate 5 nm Au NPs taken post-reaction. The atomic percentages of Bi, I, and Au from EDS measurements are shown in the table. **Reaction conditions resulting in Au NPs analyzed:** 5 nm Au NPs; T_1 = 320 °C / T_2 = 270 °C temperature setting; 4:3 Bi:I precursor ratio; 78 s.c.c.m. Ar/H_2 (5%) gas flow rate; and 5 minutes reaction time.

	Bi %	**I %**	**Au %**
Particle 1	97.2	2.4	0.4
Particle 2	97.4	2.4	0.0
Particle 3	96.7	2.6	0.8
Particle 4	98.5	1.5	0.0
Particle 5	97.4	2.2	0.5
Particle 6	97.2	2.7	0.1
Particle 7	98.7	0.7	0.6
Particle 8	98.4	1.6	0.0
Particle 9	98.5	1.5	0.0
Particle 10	97.3	2.1	0.6
Average ± Std. Dev.	97.7 ± 0.7	2.0 ± 0.6	0.3 ± 0.3

Table S12. Elemental composition of the resulting on-substrate 100 nm Au NPs taken post-reaction for a control CVD reaction with only HgI_2 in the precursor both (no Bi). The atomic percentages of I and Au from EDS measurements are shown in the table. These results show that the presence of Bi is necessary to form a nucleation point eutectic with Au NPs that melt at lower temperatures. **Reaction conditions resulting in Au NPs analyzed:** 100 nm Au NPs; $T_1 = 320$ °C / $T_2 = 270$ °C temperature setting; only HgI_2 powder precursor; 78 s.c.c.m. Ar/H_2 (5%) gas flow rate; and 5 minutes reaction time.

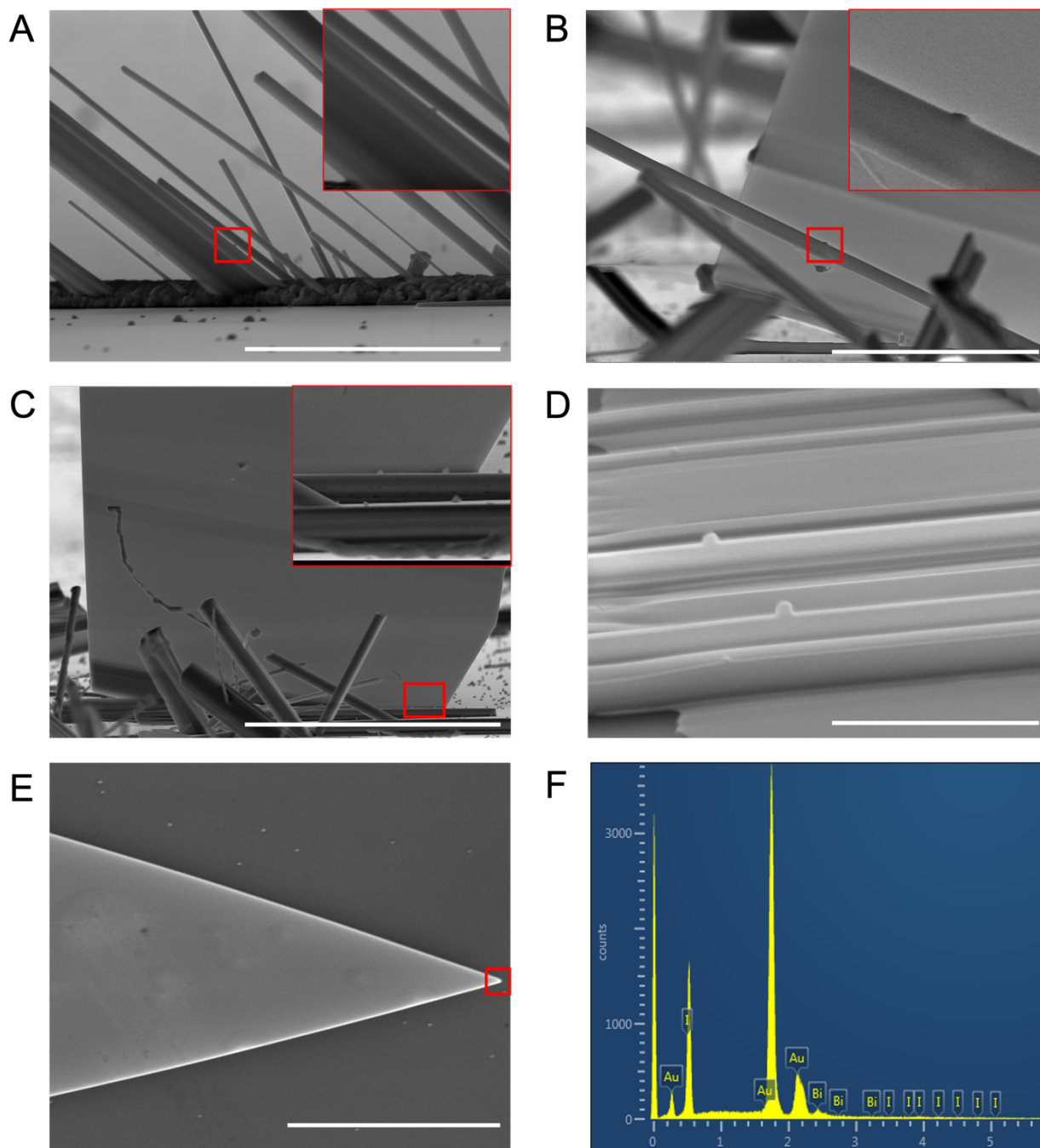| Nanoparticle	I %	Au %
Particle 1	0	100
Particle 2	0	100
Particle 3	0	100
Particle 4	2.1	97.9
Particle 5	0	100
Particle 6	0	100
Particle 7	0.8	99.2
Particle 8	0	100
Average ± Std. Dev.	0.4 ± 0.8	99.7 ± 0.8

Figure S13. (A-D) SEM images of Bi_4I_4 nanowires showing Au NPs on the surface. The micrographs were taken with the substrate at a 90° angle from the imaging plane for improved visualization. The red boxes are added as guides to the eye and represent the region of the images the insets were taken from for A, B, and C. Scale bars, (A) 4 μm, (B) 10 μm, (C) 20 μm, and (D) 5 μm. (E) SEM image of nanosheet grown from 100 nm Au NPs. Scale bar, 15 μm. (F) EDS spectrum from tip of Bi_4I_4 nanosheet, red box in (E). Percent composition 82.1% Au, 11.3% Bi, and 6.6% I.
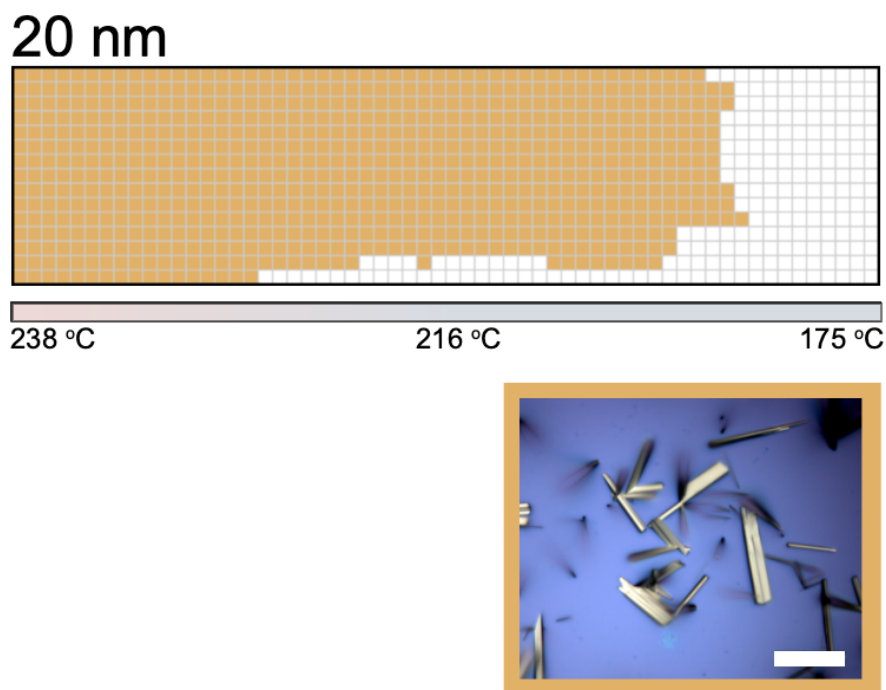
Figure S14. Substrate mapped with 1 mm^2 resolution from a CVD reaction using a growth substrate with 10x dilution of 20 nm Au NPs. The light brown squares represent the regions where Bi$_4$I$_4$ nanowires or nanoribbons were found. The white squares represent the regions of the substrate where no nanostructures were observed. Diluting 20 nm Au NPs resulted in much less dense deposition of Au NPs on substrate surface. Under these conditions, no quasi-2D nanosheet structures with a flag-like triangular morphology were observed on growth substrate. Scale bar, 25 μm. **Reaction conditions resulting in nanoparticles analyzed:** 20 nm Au NPs, diluted 10x; T$_1$ = 320 ^{o}C / T$_2$ = 270 ^{o}C temperature setting; 4:3 Bi:I precursor ratio; 78 s.c.c.m. Ar/H$_2$ (5%) gas flow rate; and 5 minutes reaction time.
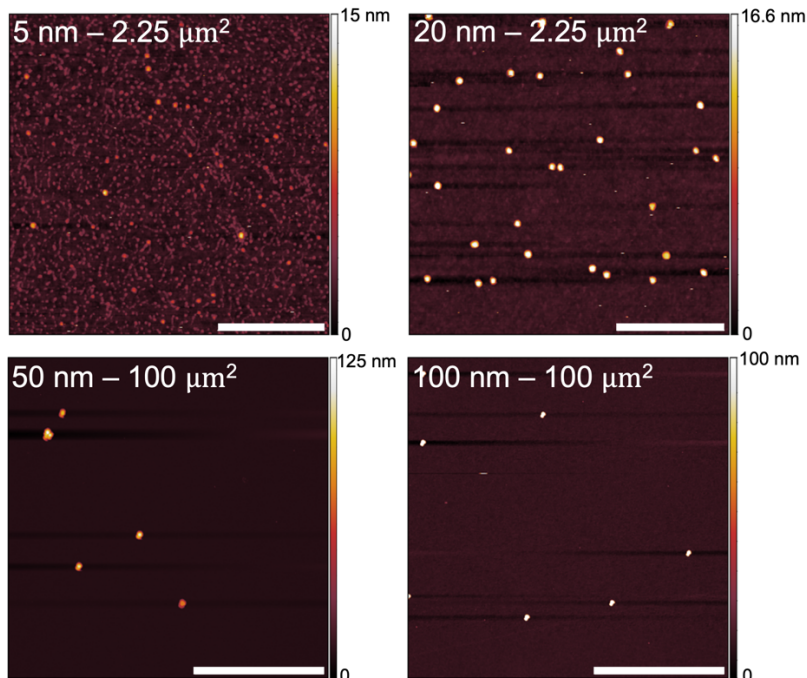
Figure S15. Representative AFM scans of SiO_2/Si substrates dropcasted with 5 nm, 20 nm, 50 nm, and 100 nm Au NPs. Scale bars, (top left) 500 nm, (top right) 500 nm, (bottom left) 4 µm, and (bottom right) 4 µm.

Table S13. Corresponding concentration of Au NPs available from BBI Solutions (Au NP supplier) and the average Au NP deposition density on the SiO_2/Si substrate.

Au NP Diameter (nm)	NPs / mL	NPs / µm² on SiO_2/Si	Gold Volume (nm³) / µm² on SiO_2/Si
5	5×10^{13}	20 ± 5	1.76×10^3
20	7×10^{11}	10 ± 3	1.13×10^5
50	4.5×10^{10}	0.11 ± 0.04	1.76×10^6
100	5.6×10^9	0.09 ± 0.09	1.41×10^7

Au NPs with 5 nm, 20 nm, 50 nm, and 100 nm diameters were dropcast on SiO_2/Si substrates in a method identical to that described previously in the SI. Multiple AFM scans (4-6 scans) were then taken of 10 µm x 10 µm areas from the SiO_2/Si substrates decorated with different diameter Au NPs. To aid in visualization, the scans shown of the 5 nm and 20 nm Au NPs are of 1.5 µm x 1.5 µm areas. The density of Au NPs on the substrate surface was calculated for each of the different diameter Au NPs. It is worth mentioning that the AFM scans of the 100 nm Au NPs revealed the 100 nm Au NPs tend to cluster on the substrate surface in comparison to the 5 nm, 20 nm, and 50 nm Au NPs which showed more uniform deposition patterns. Multiple 10 µm x 10 µm areas for the 100 nm Au NPs had no NPs at all.

The data collected here sheds light on the proposed nanosheet growth mechanism. The density of Au NPs on the substrate surface is seen to increase with decreasing Au NP diameter. The density of Bi_4I_4 nanosheet growth also increases with decreasing Au NP diameter from 100 nm to 50 nm to 20 nm. These two trends perfectly match until we reach the 5 nm diameter Au NP.

Although the 5 nm Au NPs are observed to have the greatest density on the substrate surface, CVD growths of Bi_4I_4 nanostructures on 5 nm diameter Au NPs produced the *least* dense growth of Bi_4I_4 nanosheets. If the growth of Bi_4I_4 nanosheets were solely dependent on Au NP density, the CVD growths of Bi_4I_4 on 5 nm diameter Au NPs should produce the most nanosheets. Furthermore, if the growth of 2D nanosheets were driven by density of NP deposition, the aggregation behavior observed in the 100 nm Au NP deposition should also have produced regions of dense nanosheet growth. However, this increased growth of 2D sheets was not observed. From this data we can conclude that although the number of NPs / μm^2 may influence the growth of Bi_4I_4 nanosheets, the trend cannot be solely explained by density alone.

Assuming perfectly spherical Au NPs with fcc packing, the Au NP volume (nm^3) / μm^2 on the substrate surface was also calculated. It can clearly be seen that the volume of Au NP / μm^2 on SiO_2/Si decreases as the diameter of the Au NP decreases. As discussed in the *Main Text*, we do not discount the possibility that the greater volume of gold in the 100 nm and 50 nm Au NP loadings may influence the growth of BiI_3 observed in the colder regions of these growth substrates (Fig. 2c).
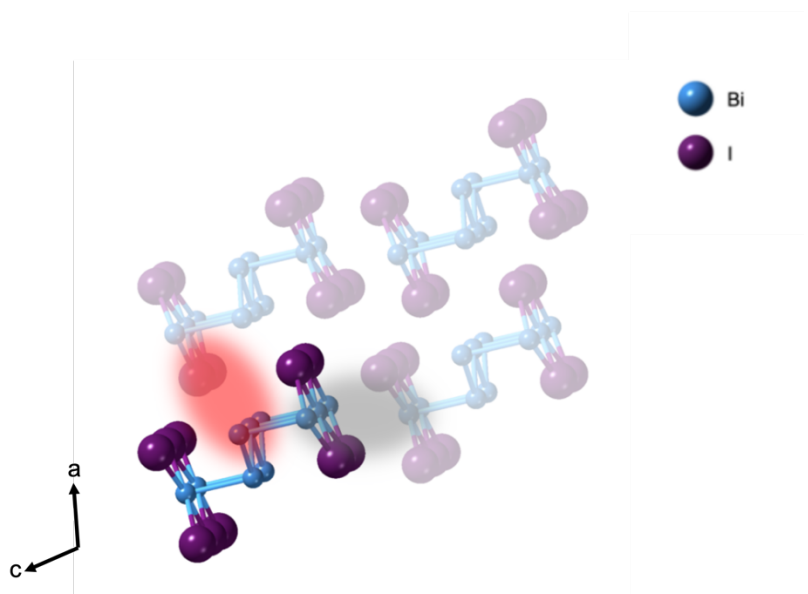
Figure S16. Nearest-neighbor Bi—I interactions in Bi_4I_4. Crystal structure representation of a $[Bi_4I_4]_n$ chain (opaque atoms) highlighting the closest Bi—I nearest neighbor interactions across adjacent chains (translucent atoms). The red region highlights the probable interaction of Bi *6s* lone pairs of the three-coordinate Bi atom in the middle of the chain with the more electronegative I atom on an adjacent chain. The orientation of this lone pair coincides with the [100] crystallographic direction and zone axis and is expected to be the strongest vdW interaction across the various crystallographic axes around the $[Bi_4I_4]_n$ chain. The gray region, on the other hand, highlights the weaker vdW interaction that exists between the adjacent chains between the five-coordinate Bi atoms oriented along the [001] crystallographic direction. The colors used in this schematic illustration are the same as the colors of the bond distances shown in Fig. S16.
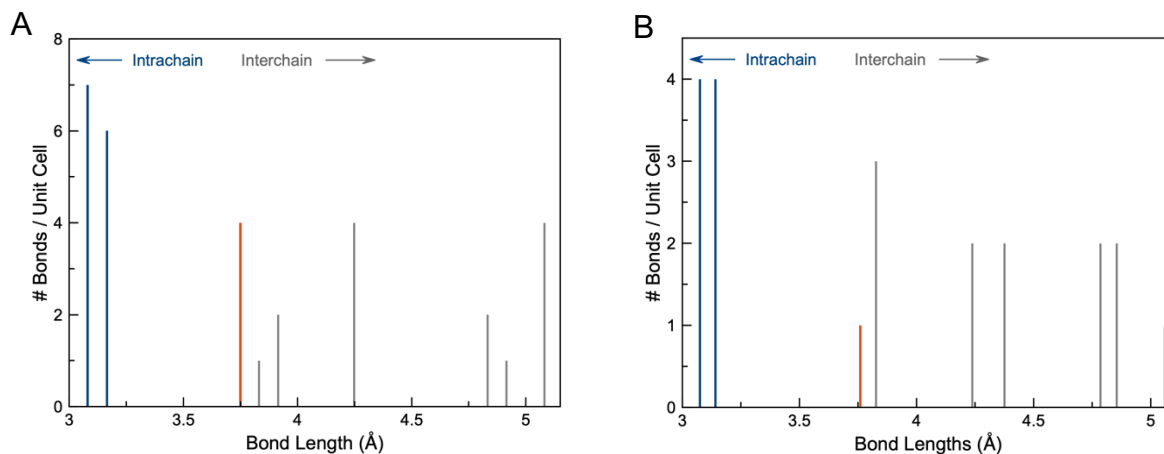
Figure S17. Graphical representation of the Bi—I distances including both vdW and covalent interactions found in the unit cell for α-Bi$_4$I$_4$ (A) and β-Bi$_4$I$_4$ (B). The blue lines indicate covalent bonds along the [Bi$_4$I$_4$]$_n$ chain while the gray lines indicate Bi—I distances that extend beyond the chain (e.g. vdW interactions). The red lines highlight the shortest inter-chain Bi—I distances which correspond to stronger vdW interactions as compared to the other inter-chain vdW interactions. This shorter Bi—I distance coincides with the orientation of the Bi lone pair pointed towards an I atom in the adjacent chain along the [100] direction as depicted in the red region in Fig. S15.

Table S14. Size measurements of CVD-grown Bi_4I_4 nanosheets using different Bi:I precursor ratios. The "short axis" is the widest point across the triangular nanosheet while the "long axis" is the longest distance from the base of the triangular nanosheet to the tip. All measurements were obtained from tilted SEM images of Bi_4I_4 nanosheets. Nanosheets grown from a 4:2 Bi:I precursor ratio have an average aspect ratio ($\frac{long\ axis}{short\ axis}$) of 10(3), while nanosheets grown from a 4:3 Bi:I precursor ratio have an average aspect ratio of 2.3(4).

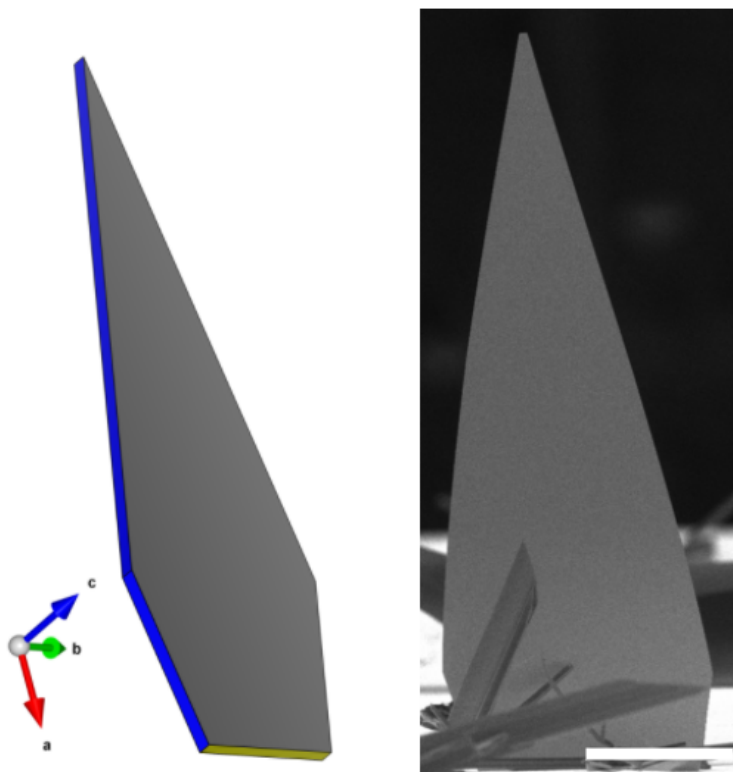| 4:2 Bi:I			4:3 Bi:I		
Short Axis (μm)	Long Axis (μm)	Ratio	Short Axis (μm)	Long Axis (μm)	Ratio
13.2	101.4	7.7	59.0	138.4	2.4
10.6	78.2	7.4	74.1	200.2	2.7
8.2	92.0	11.2	76.1	136.9	1.8
8.3	108.4	13.0	33.0	72.8	2.4

Figure S18. (left) Crystal habit representation of Bi_4I_4 with facets bound by (001), (110), and (100) surfaces depicted in gray, blue, and yellow surfaces, respectively. The model was simulated using VESTA software by propagating Miller planes with symmetry considerations imposed by the Bi_4I_4 crystal structure. (right) SEM image of a CVD-grown Bi_4I_4 nanosheet catalyzed by an Au NP. The morphology of the nanosheets derived from CVD synthesis closely resembles the expected crystal habit depicted on the left panel. Scale bar, 50 μm.

Supplementary References

(1) Ma, Z.; Chai, S.; Feng, Q.; Li, L.; Li, X.; Huang, L.; Liu, D.; Sun, J.; Jiang, R.; Zhai, T. Chemical vapor deposition growth of high crystallinity Sb2Se3 nanowire with strong anisotropy for near-infrared photodetectors. *Small* **2019**, *15* (9), 1805307.

(2) Lee, J. S.; Brittman, S.; Yu, D.; Park, H. Vapor–liquid–solid and vapor–solid growth of phase-change Sb_2Te_3 nanowires and Sb_2Te_3/GeTe nanowire heterostructures. *J. Am. Chem. Soc.* **2008**, *130* (19), 6252-6258.

(3) von Schnering, H. G.; von Benda, H.; Kalveram, C. Wismutmonojodid BiJ, eine Verbindung mit Bi (0) und Bi (II). *Z. Anorg. Allg. Chem.* **1978**, *438* (1), 37-52.

(4) Newbury, D. E. Standardless quantitative electron-excited X-ray microanalysis by energy-dispersive spectrometry: what is its proper role? *Microsc. Microanal.* **1998**, *4* (6), 585-597.

(5) Wang, X.; Li, Z.; Kavanagh, S. R.; Ganose, A. M.; Walsh, A. Lone pair driven anisotropy in antimony chalcogenide semiconductors. *Phys. Chem. Chem. Phys.* **2022**, *24* (12), 7195-7202.

(6) Kyono, A.; Kimata, M.; Matsuhisa, M.; Miyashita, Y.; Okamoto, K. Low-temperature crystal structures of stibnite implying orbital overlap of Sb $5s^2$ inert pair electrons. *Phys. Chem. Miner.* **2002**, *29* (4), 254-260.

(7) Peng, Z.; Zheng, Q.; Wang, R.; Sun, L.; Wang, H.; Yuan, Y.; Xing, Y.; Yao, L.; Bi, J.; Li, W. Controllable (hk1) preferred orientation of Sb_2S_3 thin films fabricated by pulse electrodeposition. *Sol. Energy Mater. Sol. Cells* **2023**, *253*, 112208.

(8) Cordova, D.; Chua, K.; Huynh, R.; Aoki, T.; Arguilla, M. Anisotropy-Driven Crystallization of Dimensionally Resolved Quasi-1D van der Waals Nanostructures. *ChemRxiv* **2023**.

(9) Wang, X.; Wu, J.; Wang, J.; Chen, T.; Gao, H.; Lu, P.; Chen, Q.; Ding, C.; Wen, J.; Sun, J. Pressure-induced structural and electronic transitions in bismuth iodide. *Phys. Rev. B* **2018**, *98* (17), 174112.

(10) Tiwari, D.; Alibhai, D.; Fermin, D. J. Above 600 mV open-circuit voltage BiI_3 solar cells. *ACS Energy Lett.* **2018**, *3* (8), 1882-1886.